CHAPTER 5

Determining the CO Oxidation Activity of Supported Pt_3M Clusters

5.1 Introduction

The oxidation of carbon monoxide (CO) to carbon dioxide (CO_2) ($CO + O_2 \rightarrow 2CO_2$) is an ever-growing research interest due to its promising applications such as protection of platinum (Pt) electrode from CO poisoning in fuel cells [1], exhaust purification in vehicles [2], and mechanism investigation in a catalytic reaction [3-5]. In particular, the low-temperature oxidation of CO and preferential oxidation of CO in the presence of hydrogen molecule (H_2) can only be accomplished with the existence of highly efficient catalysts. Specifically, the supported transition-metals (TMs) nanoclusters (NCs) have been utilized as stable and highly efficient catalysts extensively owing to the good dispersity and strong interaction with the support [6-8]. The pioneering finding of Haruta's on the exceptional catalytic activity of oxide-supported Au nanoparticles (NPs), the oxidation chemistry of oxide-supported (MgO, TiO_2, and CeO_2) Au NPs or NCs have been investigated to a great extent, with a particular interest in the determination of active sites and activation of the CO or oxygen molecule (O_2) by the systems with higher catalytic activity [10-15]. Basically, the interaction of catalysts with reactants, their perimeter sites, strong-metal support interaction (SMSI) (attributed to charge transfer) are the main source of enhanced catalytic activity of catalysts [16-17]. For instance, Grunwaldt et al. [18] synthesized TiO_2 supported Au NPs (with a mean particle size of 2 nm), which exhibit high activity for CO oxidation at the low temperature. Meanwhile, noble TMs such as Rh, Pt, Pd, and Au supported on transition-metal oxides (TMOs) for instance Al_2O_3, ZrO_2, CeO_2, and TiO_2 [19–22] are also investigated and considered as promising catalysts for CO oxidation reaction. Although these TMs based catalysts are effective for CO oxidation, the challenges associated with these TMs based catalysts are their high cost, limited availability, and rapid deactivation hampers their commercial application on a large scale [23]. Bimetallic clusters/nanoalloys (NAs) provide the possibility to tailor the size and the composition of nanocatalyst by replacing parent TMs with the secondary TMs which retain/enhanced the catalytic

properties of the parent cluster [24−27]. The synergetic effects between different metals influence the geometrical and electronic structure [28] of the active sites of the resulting cluster, especially, the d-states, to give the enhanced catalytic properties [29-30]. A major limitation of the TMOs supported monometallic NCs is that CO and O_2 have to compete for the same binding sites over the respective supported catalysts. The higher interaction energy of CO on monometallic NCs can result in CO poisoning, which hinders the co-adsorption of O_2 and thus prevents CO oxidation. Thus, the separate binding sites of CO and O_2 are desirable [31]. Platinum-based NCs and NAs have become a fundamental topic of investigation for CO oxidation to eliminate CO poisoning [10,32]. However, the complete elimination of Pt poisoning is still unresolved and demands molecular-level insights for CO oxidation reaction. Among the TMOs, copper oxide (CuO) and cuprous oxide (Cu_2O) are featured for their high activity at low temperature for CO oxidation, owing to the multiple oxidation states [33-35]. Huang et al. [36] have separately studied the CO oxidation activities over copper (Cu), Cu_2O, and CuO, and found that Cu_2O exhibits higher activities than the other two copper species due to the propensity of Cu_2O towards valence variations is easy to release or seize O_2. A very few reports have been concerned about the CO catalytic activity on the pristine Cu_2O and metal/Cu_2O systems [23,37-39]. To the best of our knowledge, the complete CO oxidation mechanism over Pt-based bimetallic systems supported over $Cu_2O(111)$ surface is not yet reported and requires theoretical insights to avoid Pt-poisoning.

Herein, we report the role of cobalt (Co) and Au doping in the pure pyramid Pt_4 cluster supported over the $Cu_2O(111)$ surface for CO oxidation and explore the CO oxidation mechanism at an atomistic level. Designing Cu_2O-supported bimetallic NCs of Pt_3X (X = Co and Au) where the binding sites of CO and O_2 are separated is our major goal for improving CO oxidation activity and eliminating Pt-poisoning. The second objective is to study the role of interfaces in CO oxidation over Pt_4-$Cu_2O(111)$ and Pt_3X-$Cu_2O(111)$ systems.

5.2 Computational details

The plane-wave density functional theory (DFT) calculations were performed using the Quantum ESPRESSO simulation package [40-41]. We conducted the spin-polarized PBE-D3+U (Perdew–Burke–Ernzerhof functional combined with Grimme's D3 and Hubbard (U) corrections) calculations with a value of U_{eff} = 6 eV for the consideration of Cu d-states corrections [42-45]. The projector-augmented wave (PAW) method was used to represent core—valence interactions [46]. All the valence electrons (Cu:$3d^{10}4s^1$, O:$2s^22p^4$) were treated explicitly, employing a plane-wave basis with a kinetic energy cut-off of 60 Ry. A 5 × 5 × 1 Monkhorst-Pack [47] **k**-point sampling grid was used for the Brillouin zone sampling. The Marzari–Vanderbilt cold smearing [48] of 0.01 Ry was used to improve the convergence of states near the Fermi level. The geometry optimization was carried out until the residual force on each atom was smaller than 10^{-4} eV/Å. The 3 × 3 supercell for $Cu_2O(111)$ surface was modeled as periodic slabs consisting of three Cu_2O layers. The vacuum region was set to 15 Å to avoid the interactions in the z-direction between periodic images of the system. The two top-most Cu_2O layers were allowed to relax in all directions and the bottom layer of the slab was frozen. To generate the perfect $Cu_2O(111)$ surface model, the lattice parameter for the unit cell of 111 facet obtained from the optimized values calculated for bulk Cu_2O i.e., 4.21 Å is in close agreement with the previous theoretical and experimental reports [49-50]. The top and side view of the optimized structure of the $Cu_2O(111)$ surface is shown in Figure 5.1 along with the surface sites, computed bond parameters, and angle after complete geometry optimization. Our results on structural parameters are in line with the other theoretical report [51].

Energetics. The binding energies of Pt_4 and Pt_3X clusters supported on $Cu_2O(111)$ surface were computed as,

$$E_b = E_{surface+cluster} - E_{surface} - E_{cluster} \quad (5.1)$$

where $E_{surface+cluster}$ is the total energy of the cluster interacting with the surface; $E_{surface}$ and $E_{cluster}$ are the energies of the bare surface and isolated clusters, respectively. A negative value corresponds to exothermic adsorption, with more negative values corresponding to the stronger binding.

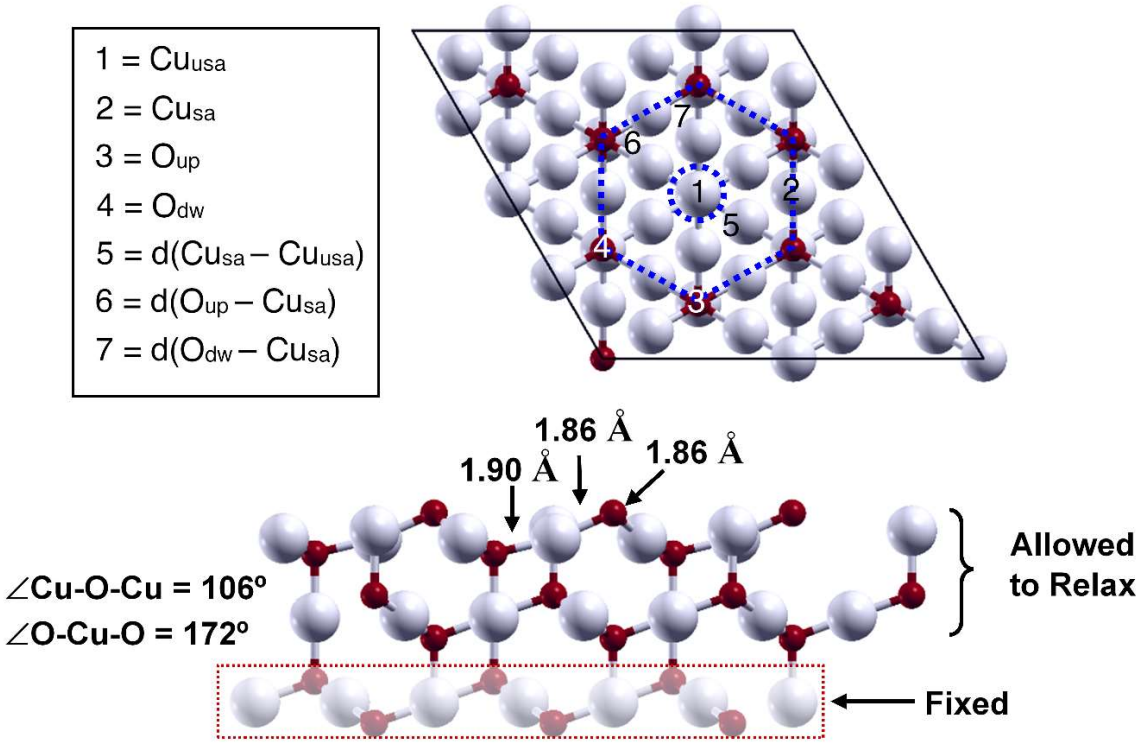

Figure 5.1: Surface sites, bond lengths and angles of $Cu_2O(111)$. Cu_{usa} and Cu_{sa} correspond to unsaturated and saturated copper surface sites, respectively. O_{up} and O_{dn} correspond to unsaturated and saturated oxygen surface sites, respectively. $d(O_{dn}–Cu_{sa})$ and $d(O_{up}–Cu_{sa})$ are the bond length of O_{dn} and O_{up} to Cu_{sa} atoms, respectively. $d(Cu_{usa}–Cu_{sa})$ is the distance between Cu_{usa} and Cu_{sa} atoms. Color key: white, Cu; and red, O.

For the molecular and atomic adsorption of reactants over Pt_4 and Pt_3X clusters supported on the $Cu_2O(111)$ surface, the adsorption energy of a given arrangement was computed as,

$$E_{ads} = E_{surface+cluster+adsorbate} - E_{surface+cluster} - E_{adsorbate} \qquad (5.2)$$

where $E_{surface+cluster+adsorbate}$ is the total energy of the adsorbate interacting with the surface supported cluster system; $E_{surface+cluster}$ and $E_{adsorbate}$ are the energies of the cluster interacting with the surface and free adsorbate in the gas phase, respectively.

The charge density difference of systems was plotted as,

$$\Delta\rho(r) = \rho(r)_{slab+cluster} - \rho(r)_{slab} - \rho(r)_{cluster} \quad (5.3)$$

Where $\rho(r)_{slab+cluster}$, $\rho(r)_{slab}$, and $\rho(r)_{cluster}$ are the charge densities distribution on the slab + cluster, pristine slab, and isolated cluster systems, respectively.

The effective charge variation (ΔQ_{eff}) was determined as,

$$\Delta Q_{eff} = Z_V - Q_{Löwdin} \quad (5.4)$$

Where Z_V is the valence charge on cluster and $Q_{Löwdin}$ is the Löwdin charge on the cluster after adsorption over a substrate.

Transition states (TSs) for each elementary reaction were located using the climbing-image nudged elastic band method (CI-NEB) [52-53]. Energy barrier (E_a) and reaction energy (ΔH) were calculated as

$$E_a = E_{TS} - E_{IS} \quad (5.5)$$

$$\Delta H = E_{FS} - E_{IS} \quad (5.6)$$

Where, E_{IS} , E_{TS} and E_{FS} respectively are energies of initial, transition states, and final states of the reaction.

5.3 Results and Discussion

5.3.1 Structural and electronic properties of $Cu_2O(111)$ surface

It is seen from Figure 5.1 that each Cu plane is sandwiched between two O planes and each of these O planes has one anion per surface unit cell and the Cu planes parallel to the (111) surface contain four Cu^+ cations per surface unit cell [54]. We have analyzed the electronic structure of the $Cu_2O(111)$ surface. In Figure 5.2(a), a bandgap of 1.0 eV is formed and can be seen from the density of states (DOS) of the $Cu_2O(111)$ surface, which is slightly underestimated in comparison to the previous report [55].

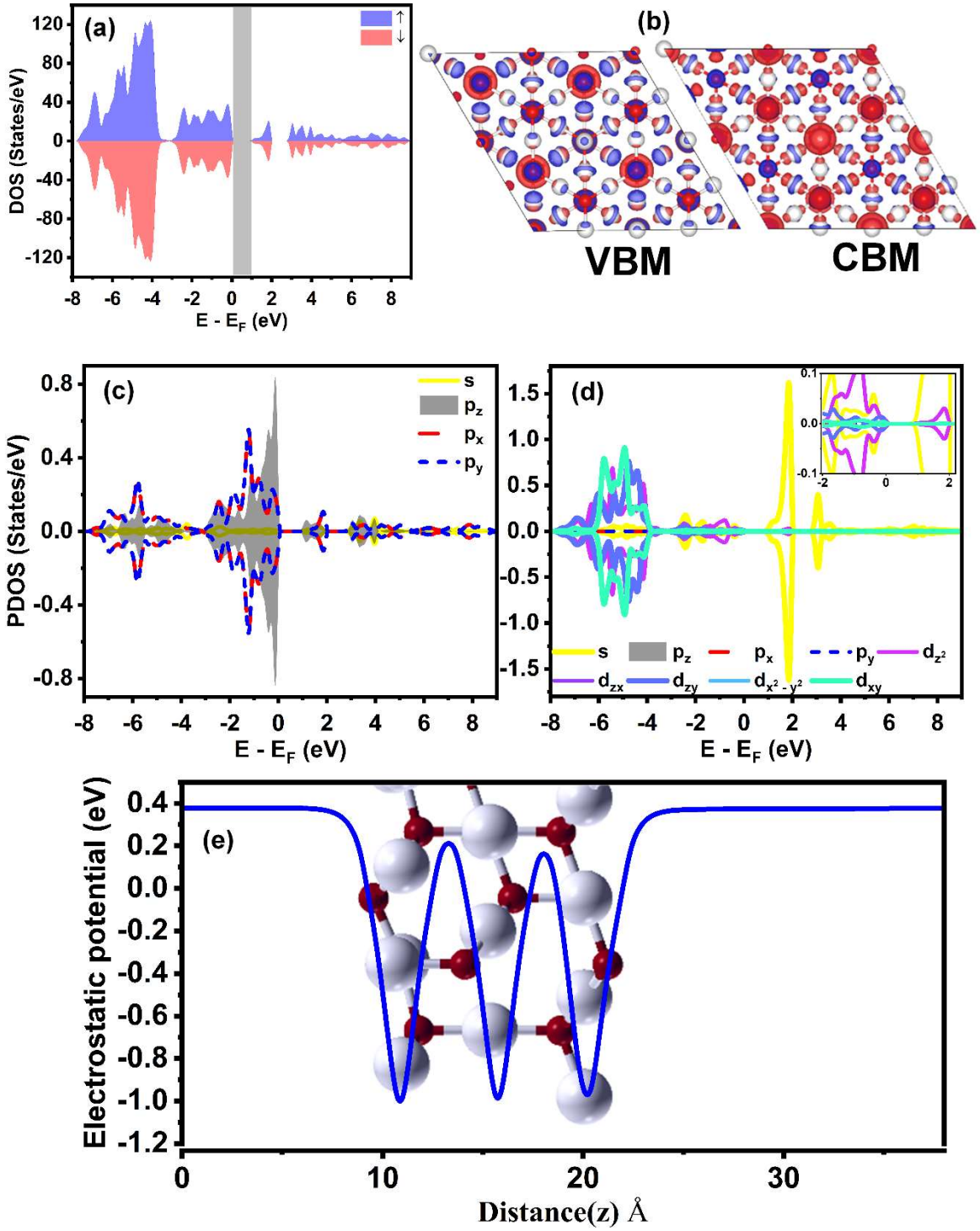

Figure 5.2: (a) The density of states of $Cu_2O(111)$ surface. (b) The charge density plot of valence band maximum (VBM) and conduction band minimum (CBM) of $Cu_2O(111)$ surface. The iso-surface value set to ±0.0003 e/Å^3. The blue and red color represent the depletion and accumulation of charge, respectively. (c-d) The projected density of state (PDOS) of O and Cu atoms, respectively. (e) The average electrostatic potential of the $Cu_2O(111)$ surface as a function of the distance in the z-direction.

The frontier orbital analysis was then carried out for valence band maximum (VBM) and conduction band minimum (CBM) states of the $Cu_2O(111)$ surface model and presented in Figure 5.2(b). For the clear view, only the top-layer atoms were illustrated. It can be seen that the surface O_{up} and O_{dw} sites are the main contributors to the valence band maximum (VBM) of the surface, implying that it is more likely to be the active site for electron-donating reactions. For conduction band minimum (CBM) analysis, the surface Cu_{usa} site majorly contributes, whereas other surface sites have a certain contribution to the surface. These facts derived from the orbital analysis of VBM and CBM are well supported by the projected density of states presented in Figure 5.2(c-d) for the O atom and Cu atom, respectively. The presented PDOS clearly defines the significant role of O-p_z orbital in VBM state and interestingly, the contribution of Cu-s state in CBM state. The in-plane averaged electrostatic potential of the $Cu_2O(111)$ surfaces as a function of the distance in z-direction was also calculated, as shown in Figure 5.2(e). The potential curve shows several dips at the position of each Cu_2O layer because the nucleus region is positively charged. It turns out that the slab region contour of the electrostatic potential of the $Cu_2O(111)$ surfaces is flat. In other words, the surface and bulk regions have similar values of electrostatic potential. Such potential acts as a smaller energy barrier for positive charge carriers, which allows the holes to move from the bulk region into the surface region. Therefore, the higher density of mobile holes in the Cu_2O (111) surface indicates its promising application as a photocatalyst [55].

5.3.2 Pt_4 and Pt_3X (X = Co & Au) supported on $Cu_2O(111)$ surface

The synergistic effect between the NCs and the oxide support plays an important role in the cluster properties and strongly affects its catalytic activity. Thus, we first investigated the structural behavior and the nature of support/cluster interaction of the $Pt_4/Cu_2O(111)$ and $Pt_3X/Cu_2O(111)$ systems before examining the catalytic mechanisms. Figure 5.3 shows the low-lying geometries and charge density difference (CDD) of $Cu_2O(111)$ surface supported Pt_4, Pt_3Au, and Pt_3Co clusters.

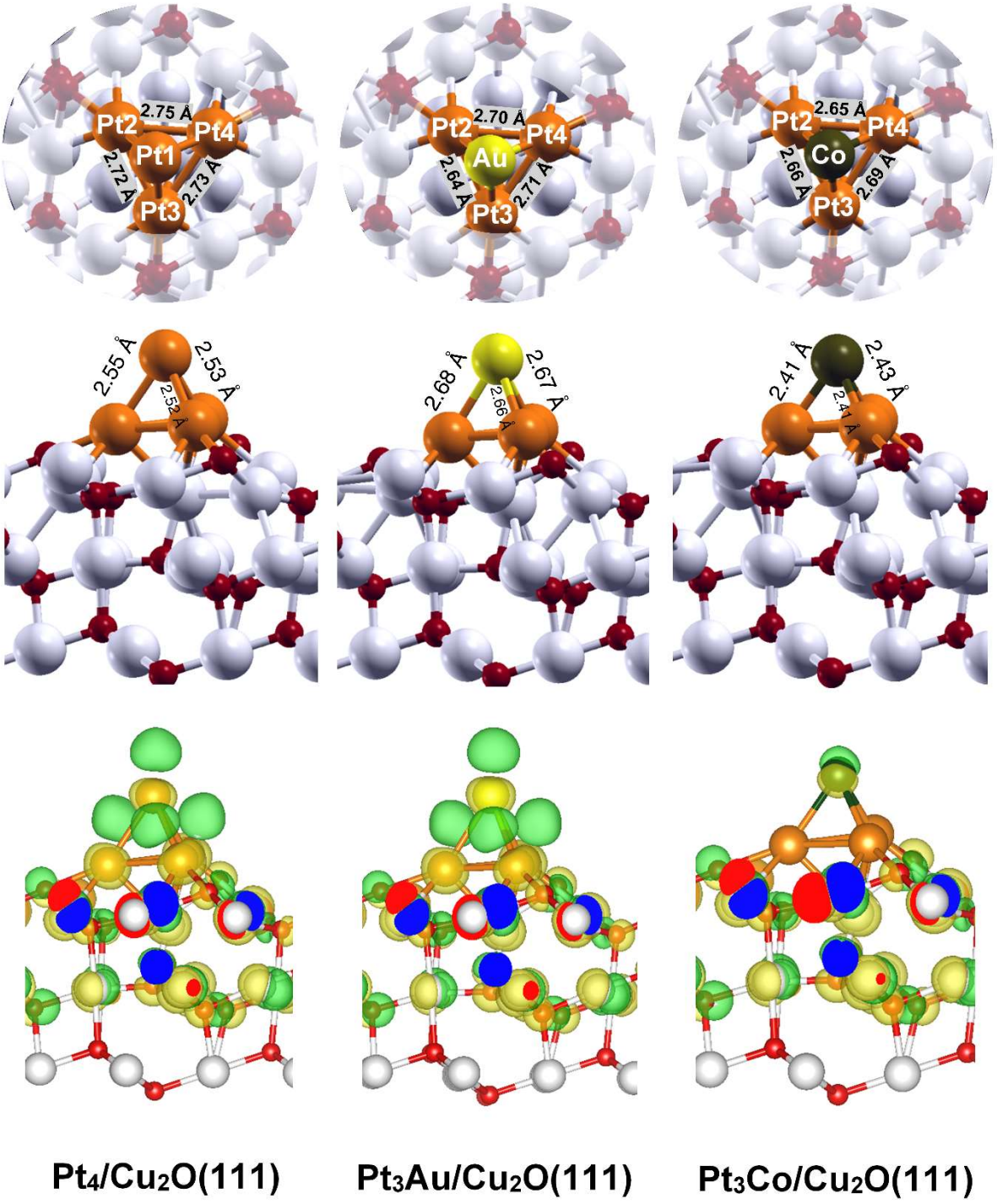

Figure 5.3: Top (upper panel) and side views (middle panel) of the optimized geometries of $Pt_4/Cu_2O(111)$, $Pt_3Au/Cu_2O(111)$, and $Pt_3Co/Cu_2O(111)$ systems. The charge density difference (CDD) of the $Pt_4/Cu_2O(111)$, $Pt_3Au/Cu_2O(111)$, and $Pt_3Co/Cu_2O(111)$ systems (bottom panel). Yellow and light green regions in CDD represent charge depletion and accumulation, respectively. The iso-surface value is set to ±0.2 e/Å^3 for CDD. Color key: white, Cu; red, O; orange, Pt; yellow, Au; and dark green Co.

On the $Cu_2O(111)$ surface (Figure 5.3), the Pt_4, Pt_3Au, and Pt_3Co clusters retain the symmetric (T_d) pyramidal structure with Pt−O and Pt−Cu bonds between the clusters/Cu_2O interface. The Pt−Pt bond length of Pt_4, Pt_3Au, and Pt_3Co are in the range of 2.52-2.75, 2.64-2.71, and 2.65-2.69 Å, respectively. The Pt−Au and Pt−Co bond lengths of Pt_3Au and Pt_3Co are in the range of 2.66-2.68 and 2.41-2.43 Å, respectively. The binding energies of Pt_4, Pt_3Au, and Pt_3Co clusters on $Cu_2O(111)$ supports were computed using Eqn. 5.1. The binding energies were -8.83, -8.68, and -7.95 eV for Pt_4, Pt_3Au, and Pt_3Co clusters, respectively. We can see that the perturbation effect on the structure of clusters is very weak after being supported over $Cu_2O(111)$ surface. The binding energy is greatest in the case of Pt_4, which is expected because the highest charge transfer was observed in this case from the surface to the Pt_4 clusters.

The spin-dependent Löwdin charge analysis shows that a net charge is transferred from $Cu_2O(111)$ surface to the Pt_4, Pt_3Au, and Pt_3Co clusters. A detailed analysis of the spin-dependent Löwdin charge analysis indicates that Pt_4 clusters lose electron density up to 0.64 e in the spin-up state while it gains up to 1.83 e electron density in the spin-down state. Contrary to this case, Pt_3Au and Pt_3Co clusters gain electron density up to 0.63 e and 0.47 e in spin-up states, respectively. The Pt_3Au and Pt_3Co clusters also gain electron density up to 0.66 e and 0.58 e in the spin-down state, respectively. These facts point out that minority spin plays an important role in the strong metal-support interaction (SMSI). It seems that all three clusters are negatively charged on $Cu_2O(111)$ support and the strongest net charge transfer is in the case of the Pt_4 cluster. In the bimetallic clusters, the Au atom gains excess electrons as compared to Co, this can be attributed to the differences in electron negativities, which are 2.54 and 1.88 for Au and Co, respectively. To picturize the interaction between considered clusters over $Cu_2O(111)$ support, the charge density distributions (CDDs) of the considered combine systems were examined using Eqn. 5.3 and plotted in Figure 5.3. These plots presented in Figure 5.3 show the strong interaction at the interface between the considered clusters and the

$Cu_2O(111)$ surface. It shows pronounced interaction between the Pt_4 and Pt_3Au clusters and $Cu_2O(111)$ support while weak interaction observed between the Pt_3Co and $Cu_2O(111)$ surface (compared to the other two cases). These findings are in agreement with the trend obtained for calculated binding energy and net charge transfer from $Cu_2O(111)$ surface to clusters.

The electronic reactivity descriptors such as *d-band* center (averaged energy positions of all d orbitals) and fractional filling of *d-band* are often considered as a key quantity to understand the catalytic activity of noble metal catalysts for instance transition-metal surfaces, transition-metal oxide surface, nanoclusters/nanoalloys and supported NCs/NAs. Therefore, the modification in the catalytic activity can be better understood by examining the electronic structure of the considered systems [56-57]. Table 5.1 presents the calculated spin-dependent *d-band* center (ε_d) and fractional filling of *d-band* (f_l) of each atom present in cluster supported over $Cu_2O(111)$ surface. The value of the calculated ε_d represents the distance of the ε_d from the Fermi level. If the ε_d is far below the Fermi level than a smaller number of empty antibonding states are available to react with an adsorbate. If the ε_d is closer to the Fermi level then a large number of empty antibonding states are available to react with an adsorbate. For $Cu_2O(111)$ supported Pt_4 cluster, the value of ε_d for both spin up and spin down states of Pt1 atom (see Figure 5.3 for reference) were found similar (also $f_{l\uparrow} = f_{l\downarrow}$) and are close to Fermi level compared to Pt atoms which are directly attached to the $Cu_2O(111)$ surface. Thus, this Pt1 atom will be considered as the preferred site in the following investigation for the adsorption of CO due to the higher number of availabilities of antibonding states. In the case of $Pt_3Au/Cu_2O(111)$ systems, the value of $\varepsilon_{d\uparrow}$ and $\varepsilon_{d\downarrow}$ ($f_{l\uparrow} > f_{l\downarrow}$) of Pt_3 atom is closer to the Fermi level than that for Pt2 and Pt4 atoms. The value of $\varepsilon_{d\uparrow}$ and $\varepsilon_{d\downarrow}$ of Au are found almost identical (also $f_{l\uparrow} = f_{l\downarrow}$) and are far below that of the Pt3 site. This information forecasting the chance of strong adsorption of CO on the Pt3 site.

Table 5.1 Calculated *d-band* center (ε_d, eV) and *d-band* filling (f_l, eV) for both the spin-up and the spin-down state of each atom of the clusters supported over $Cu_2O(111)$ surface.

Systems	$\varepsilon_{d\uparrow}$	$\varepsilon_{d\downarrow}$	$f_{l\uparrow}$	$f_{l\downarrow}$
Pt_4				
Pt1	-2.01	-2.01	0.90	0.90
Pt2	-2.51	-2.51	0.88	0.89
Pt3	-2.39	-2.36	0.92	0.85
Pt4	-2.53	-2.55	0.85	0.92
Pt_3Au				
Au	-2.78	-2.79	0.98	0.97
Pt2	-2.26	-2.22	0.93	0.85
Pt3	-2.20	-2.15	0.94	0.85
Pt4	-2.29	-2.27	0.92	0.87
Pt_3Co				
Co	-1.47	-1.35	0.79	0.76
Pt2	-2.67	-2.68	0.88	0.90
Pt3	-2.63	-2.64	0.86	0.93
Pt4	-2.71	-2.71	0.88	0.90

However, the applicability of the ε_d is questionable for the Ag and Au systems. Thus, both Pt3 and Au sites will be considered to investigate of CO adsorption mechanism in this present work. The $\varepsilon_{d\uparrow}$ and $\varepsilon_{d\downarrow}$ of the Co atom in $Pt_3Co/Cu_2O(111)$ system are very closer to the Fermi level than that of the Pt atoms those are directly attached to the $Cu_2O(111)$ surface, which indicates the more availability of Co antibonding states than those of the Pt atoms (utilized their available antibonding states causes a downshift of the Pt ε_d compared to that of Co site). Also, the $f_{l\uparrow}$ and $f_{l\downarrow}$ of the Co atom is lower than those of Pt atoms. Hence, the Co site can be predicted as the preferred site for the adsorption of CO. To gain more insight into the electronic structure of the cluster/surface interaction, a detailed analysis of the frontier orbitals has been performed through the examination of the projected density of states (PDOS), which includes the contribution of s, p, and d orbitals components. Figures 5.4(a-e)-5.6(a-e) display the total density of states (DOS), frontier orbitals (HOMO and LUMO states), and PDOS of $Pt_4/Cu_2O(111)$ and $Pt_3X/Cu_2O(111)$ systems.

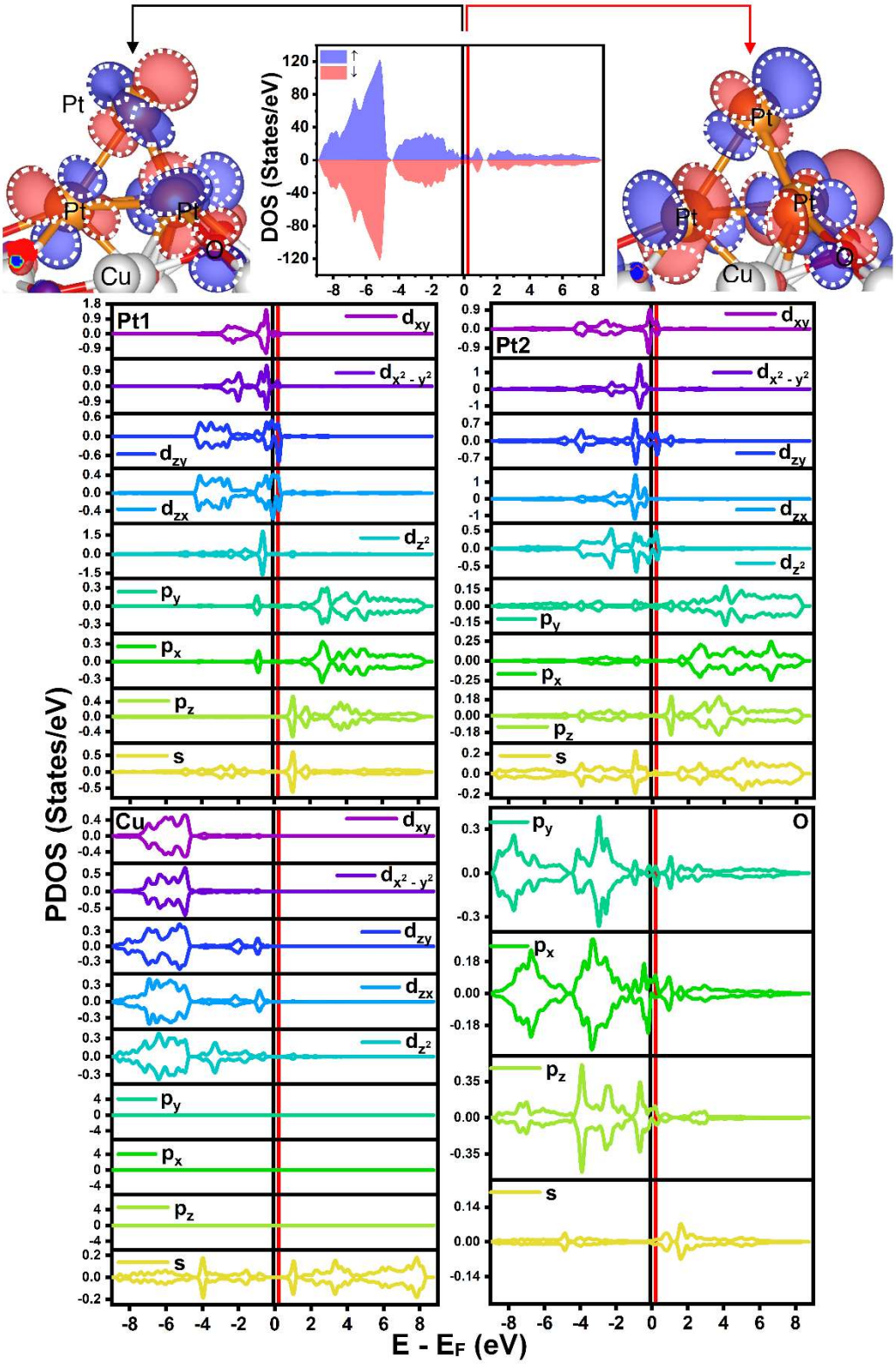

Figure 5.4: (a) The total density of states of the $Pt_4/Cu_2O(111)$ system with the HOMO and LUMO orbitals where charge depletion indicated by blue region and accumulation of charge indicated by red region. The iso-surface value is set to ±0.0007 e/Å^3. (b-e) Atom-wise projected density of states of the $Pt_4/Cu_2O(111)$ system. The black and red lines indicate the HOMO and LUMO levels. The Fermi energy is set to zero.

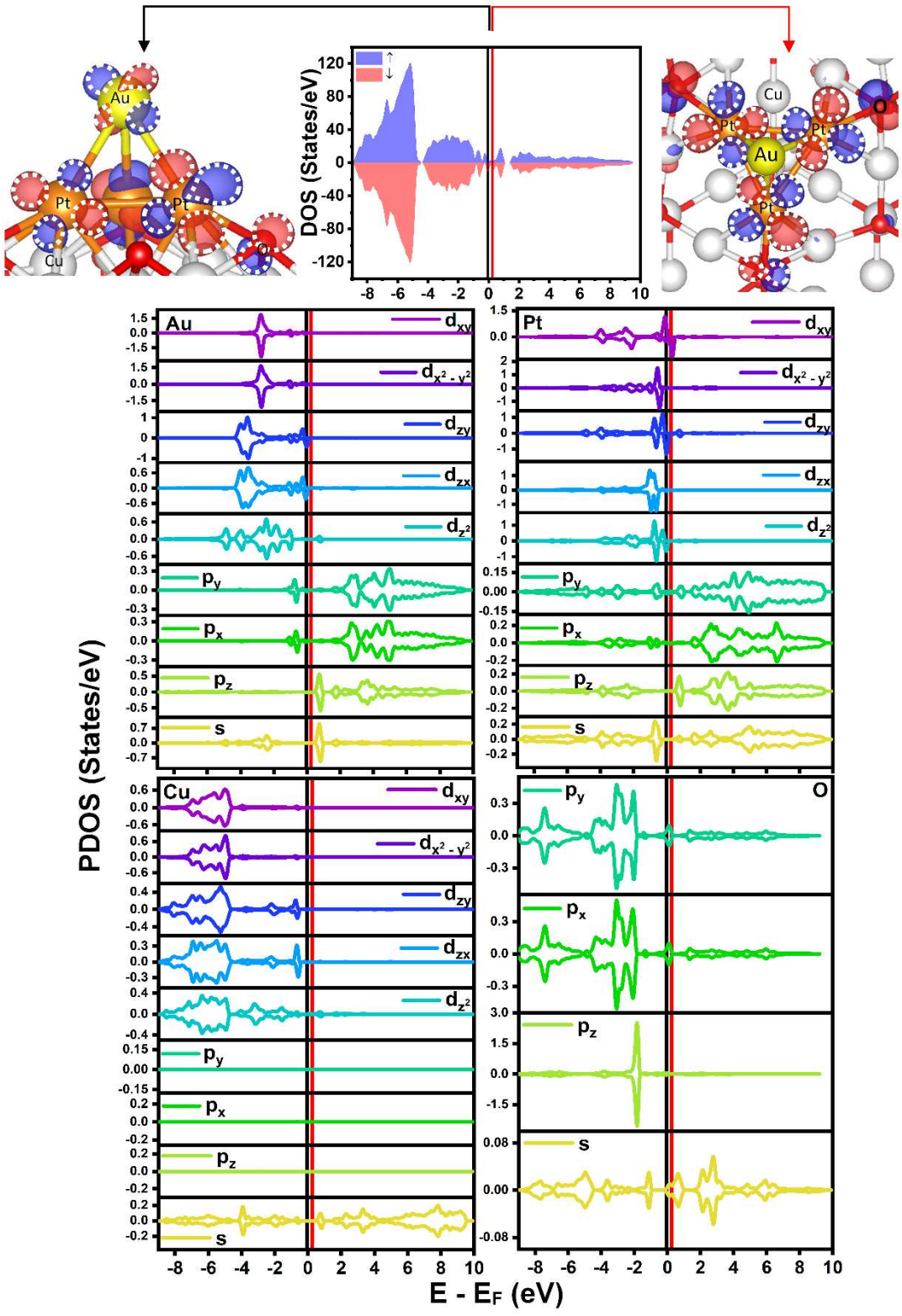

Figure 5.5: (a) The total density of states of the $Pt_3Au/Cu_2O(111)$ system with the HOMO and LUMO orbitals where charge depletion indicated by blue region and accumulation of charge indicated by red region. The iso-surface value is set to ±0.004 e/Å^3. (b-e) Atom-wise projected density of states of the $Pt_3Au/Cu_2O(111)$ system. The black and red lines indicate the HOMO and LUMO levels. The Fermi energy is set to zero.

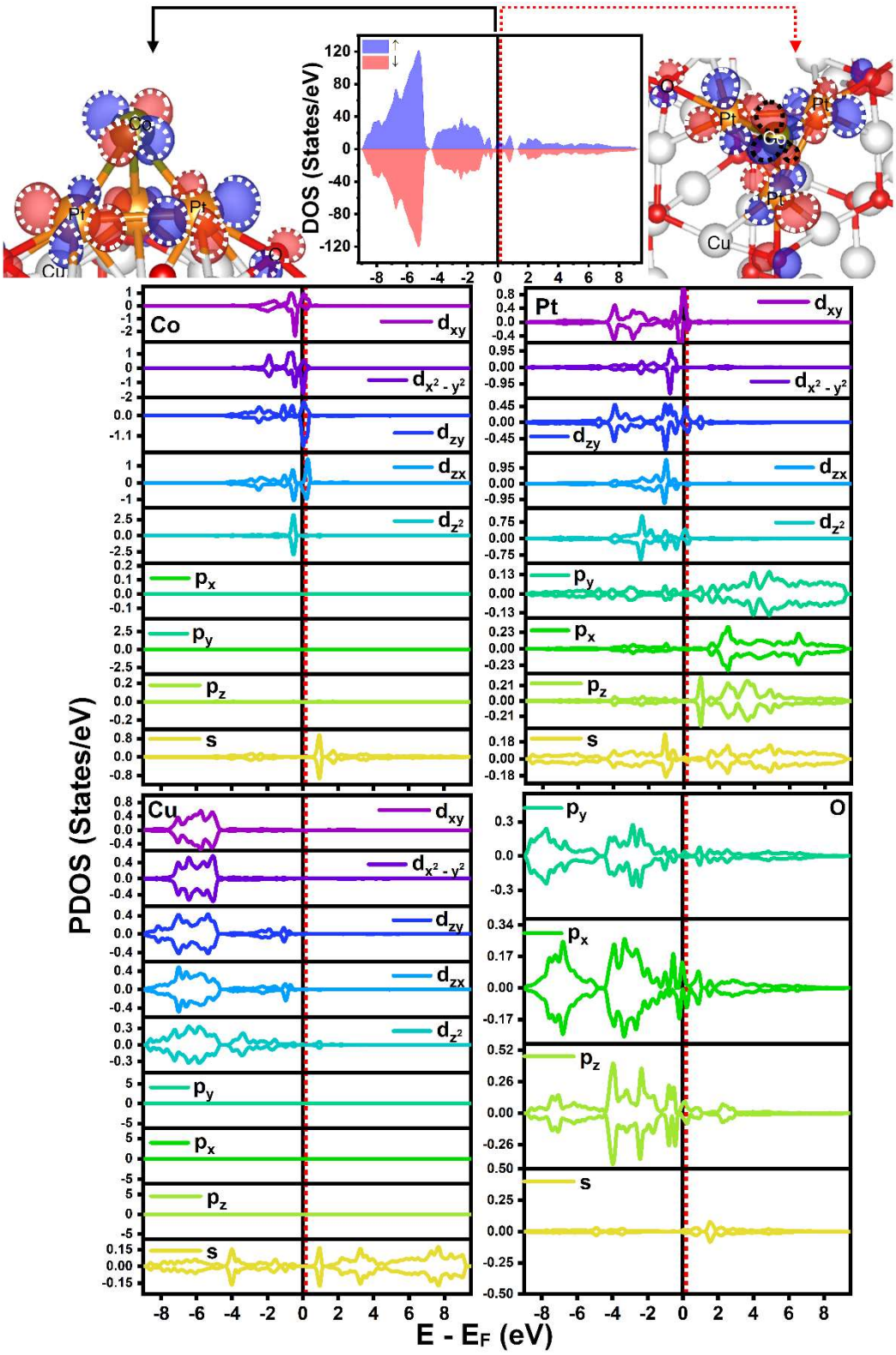

Figure 5.6: (a) The total density of states of the $Pt_3Co/Cu_2O(111)$ system along with the molecular orbitals of the HOMO and LUMO states. The iso-surface value is set to ±0.002 e/Å^3. (b-e) Atom-wise projected density of states of the $Pt_3Co/Cu_2O(111)$ system. The black and red lines indicate the HOMO and LUMO levels. The Fermi energy is set to zero.

From the PDOS of Pt, Au, and Cu atoms of the cluster along with the PDOS of Cu and O atoms of the $Cu_2O(111)$ surface, the metallic nature of these systems identified when the considered clusters supported over $Cu_2O(111)$ surface as can be seen from Figure 5.4(a) - 5.6(a). We also examined the frontier orbitals for each case which are presented in the uppermost panel of Figure 5.4(a)-5.6(a) in the form of HOMO and LUMO states. Seeing that from Figure 5.6(b-c), the contributions of d_{zx} and d_{zy} orbitals of Pt1 atom and d_{xy} orbitals of Pt2 atom are the most prominent in the HOMO state, while the contributions of d_{zx} and d_{zy} orbitals of Pt1 atom and d_{zy} along with the d_{z^2} orbitals of Pt2 atom are the most prominent in the LUMO state of $Pt_4/Cu_2O(111)$ system. In the case of the $Pt_3Au/Cu_2O(111)$ system, the significant contributions of d_{zx} and d_{zy} orbitals of Au atom and d_{xy} along with d_{zy} orbitals Pt2 atom detected in the HOMO state. Notably, the contribution of d-orbitals of Au is nil while the contribution of d_{xy} orbitals of Pt2 atoms is noticeable in the LUMO state (see Figure 5.5(b-c)). It is seen from that the contributions of d_{zy} and $d_{x^2-y^2}$ orbitals of Co atom and d_{xy} orbitals of Pt2 atom dominates the HOMO state and LUMO state dominated by the d_{zx} and d_{xy} orbitals of Co atom and d_{zy} orbitals Pt2 atom in the case of $Pt_3Co/Cu_2O(111)$ system (see Figure 5.6(b-c)). For all the cases, the p-orbitals of O atoms (support) also consume visible weight.

5.3.3 CO adsorption on supported clusters

As discussed in section 5.2, the adsorption of CO performed over the (1) Pt1 atom of $Pt_4/Cu_2O(111)$ system, (2) Au and Pt2 atoms of $Pt_3Au/Cu_2O(111)$ system, and (3) Co and Pt2 atom of $Pt_3Co/Cu_2O(111)$ system. The adsorption energies for CO on Pt_4, Pt_3Au, and Pt_3Co on $Cu_2O(111)$ were calculated to be -2.41, -1.98, and -2.24, respectively. The optimized geometries of CO adsorbed systems are presented in Figure 5.7. Our findings on CO adsorption over supported Pt_3Au and Pt_3Co clusters indicate that CO energetically prefers the Au and Co atom as the adsorption site.

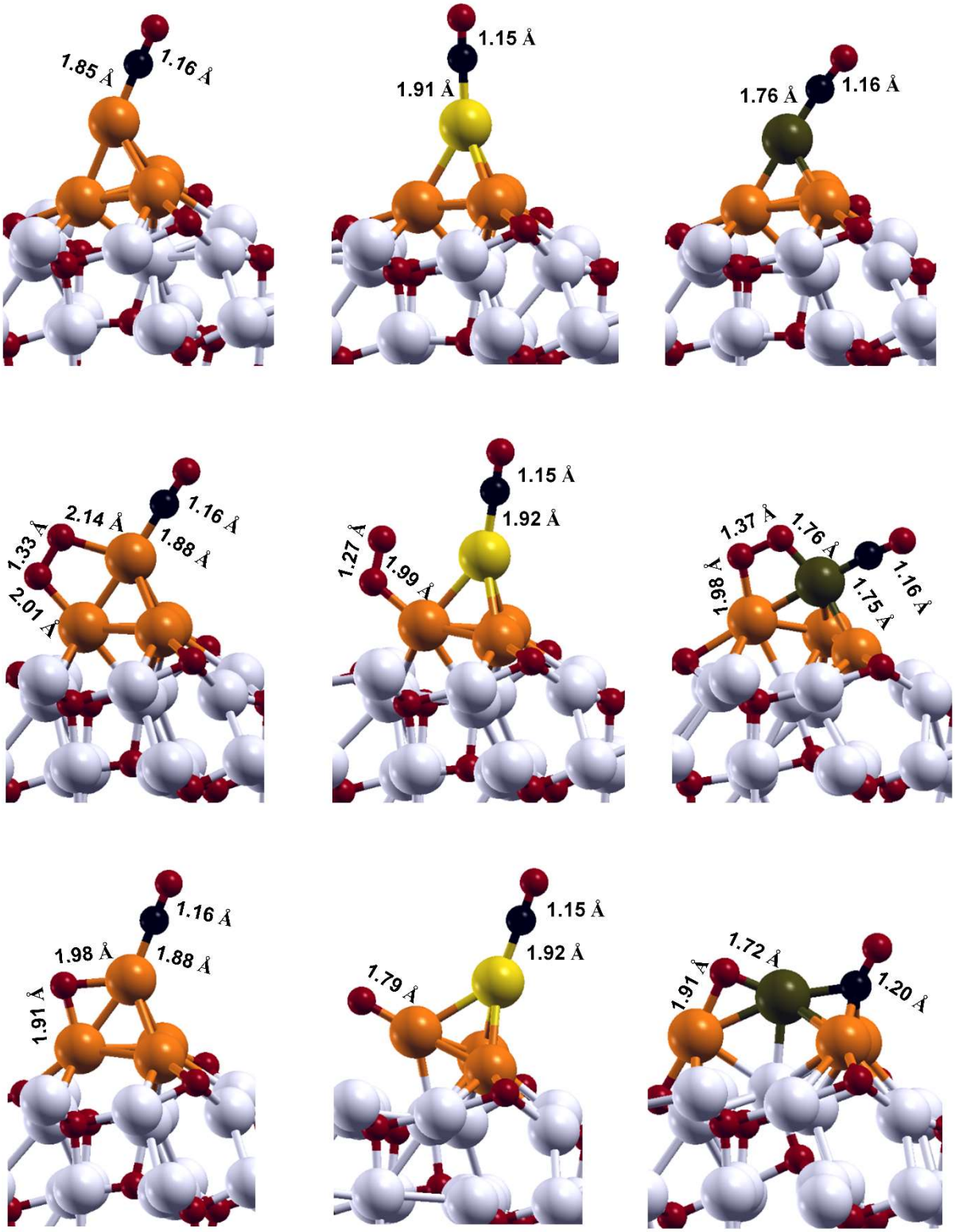

Figure 5.7: The optimized geometry and structural parameter (bond length) of CO (upper panel), CO + O_2 (middle panel), and CO + O (bottom panel) over $Pt_4/Cu_2O(111)$ and $Pt_3X/Cu_2O(111)$ (X = Au and Co) systems. Color key: white, Cu; red, O; black, C: orange, Pt; yellow, Au; and dark green, Co.

As predicted in section 5.2, the *d-band* center position relative to Fermi energy is a good indicator of the favorable adsorption site over transition metal-based heterogeneous catalyst (except Au and Ag) and an effective method for the rational design of catalysts.

5.3.4 L-H reaction mechanism for CO oxidation

The Langmuir-Hinshelwood (L-H) mechanism for the CO oxidation by molecular O_2 initiated by the co-adsorption of CO and O_2(2O) has been vastly reported [10,58-59]. Therefore, the reaction barrier for the L-H mechanism is quite inferior to the desorption energies of CO and O_2 [60-61]. In the L-H mechanism, the co-adsorption of CO + O_2(2O) over the supported catalysts is the very first and considered a crucial step for CO oxidation analogous to previous reports [60-61]. The most stable co-adsorption configurations for CO + O_2 and CO + O over $Pt_4/Cu_2O(111)$ and $Pt_3X/Cu_2O(111)$ systems are shown in Figure 5.7. For CO + O_2, the preferable co-adsorption pattern involves the top site for CO and the bridge site for O_2 on Pt_4 and Pt_3X. For CO + O_2, the favorable co-adsorption configuration involves the top site for CO, superoxo state of O_2 on the supported Pt_3Au cluster, and peroxo state of O_2 on the supported Pt_4 and Pt_3Co clusters. For CO + O, the favorable co-adsorption configuration involves the top site for CO over supported Pt_4 and Pt_3Au clusters and the hollow site of the supported Pt_3Co cluster. The single oxygen atom prefers to adsorb on the bridge site of supported Pt_4 and Pt_3Co clusters and top site of supported Pt_3Au cluster. The co-adsorption energy of CO + O_2 and CO + O over considered systems is calculated using Eqn. 5.2. The value of co-adsorption energy for CO + O_2 is -3.81 eV, -2.86 eV and -4.17 eV on supported Pt_4, Pt_3Au and Pt_3Co clusters, respectively. The value of co-adsorption energy for CO + O is -6.94 eV, -6.30 eV, and -8.55 eV on supported Pt_4, Pt_3Au, and Pt_3Co clusters, respectively. For ease of understanding, the L-H pathway is divided into two halves for each system and are shown in Figures 5.8-5.10. The symbol (*) and (g) indicate the adsorbed and free state of reactants, respectively.

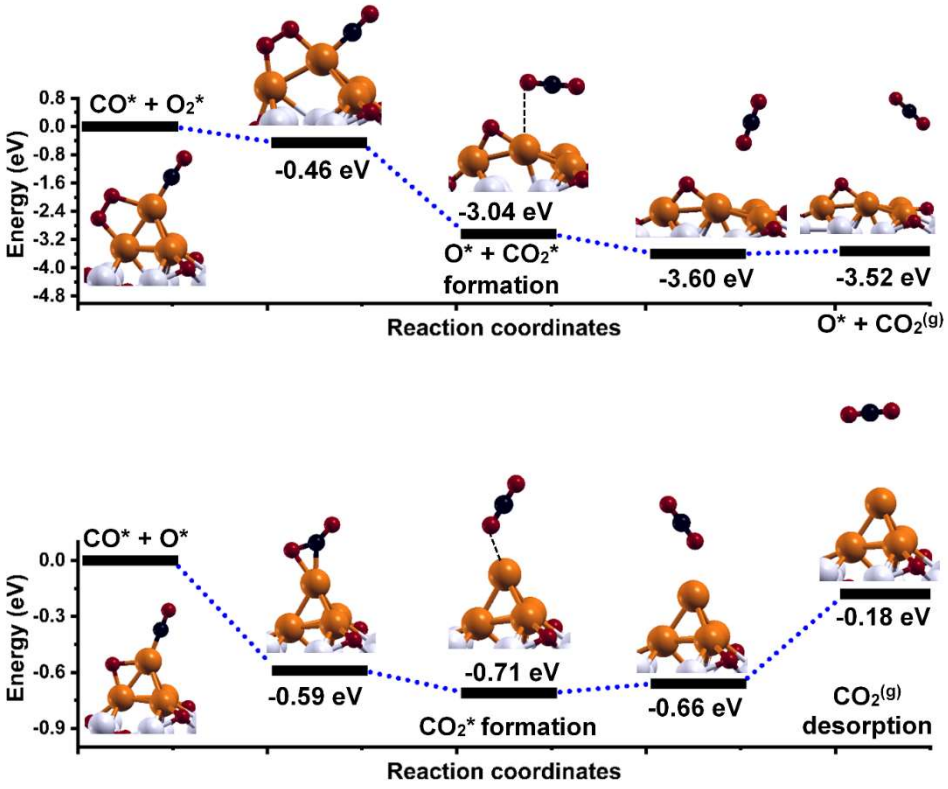

Figure 5.8: The complete L-H mechanism reaction pathway for CO oxidation onto the $Pt_4/Cu_2O(111)$ system. Color key: white, Cu; red, O; black, C; and orange, Pt.

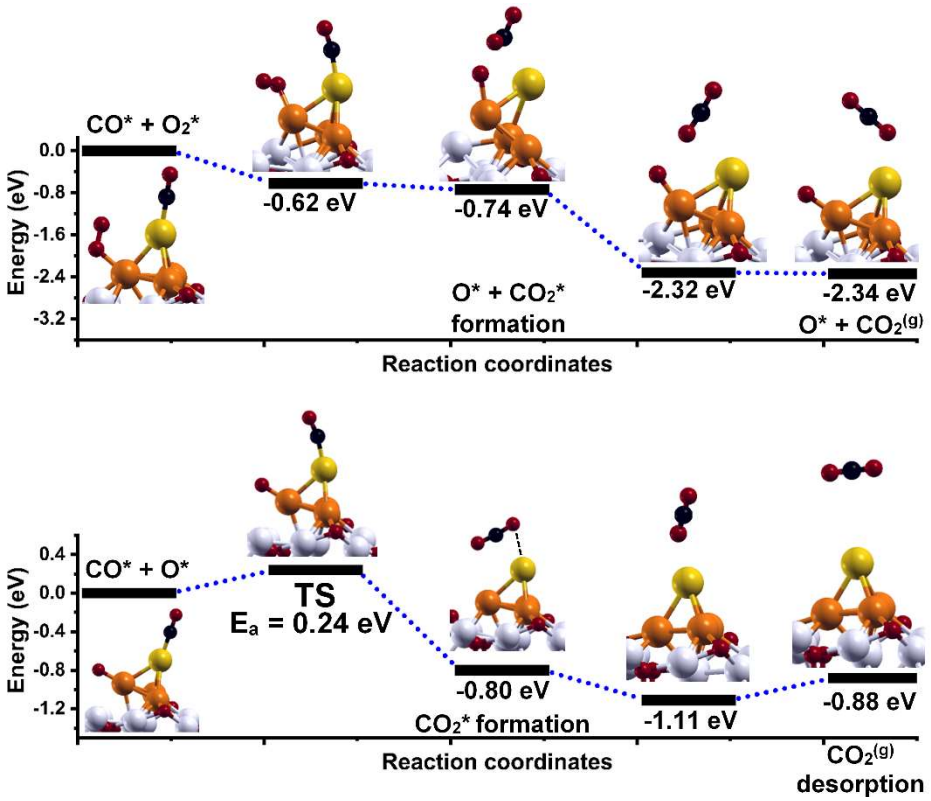

Figure 5.9: The complete L-H mechanism reaction pathway for CO oxidation onto the $Pt_3Au/Cu_2O(111)$ system. TS indicates a transition state. Color key: white, Cu; red, O; black, C: orange, Pt; and yellow, Au.

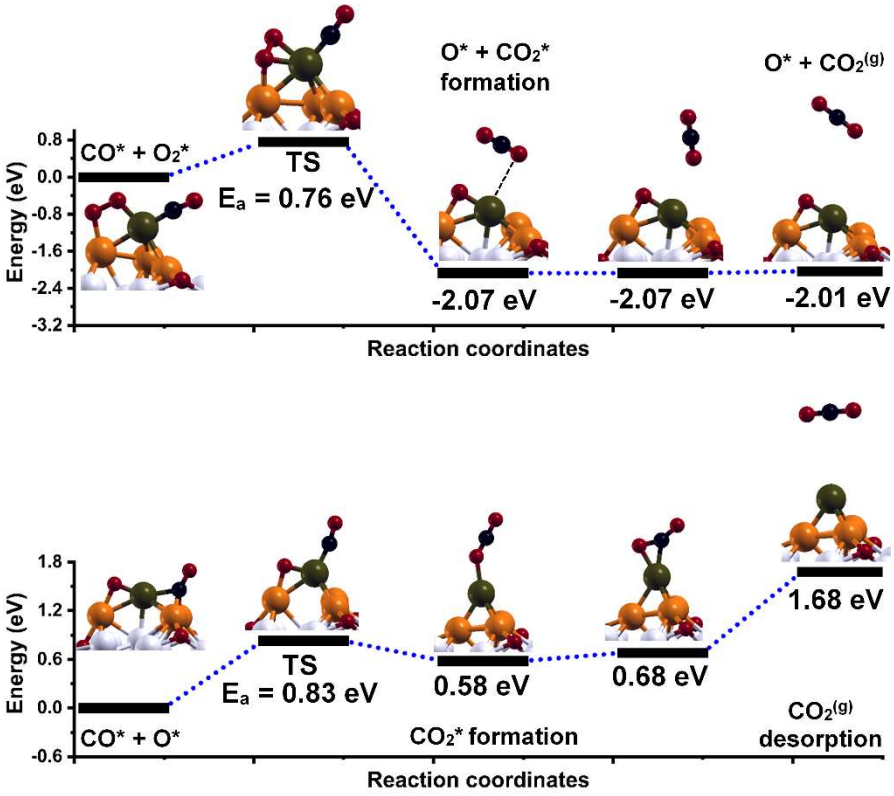

Figure 5.10: The complete L-H mechanism reaction pathway for CO oxidation onto the $Pt_3Co/Cu_2O(111)$ system. TS indicates a transition state. Color key: white, Cu; red, O; black, C: orange, Pt; yellow, Au; and dark green, Co.

It can be seen from Figures 5.8-5.10 that the first half of the CO oxidation ($CO^* + O_2^* \rightarrow CO_2^{(g)} + O^*$) reaction involves the breaking of the peroxo bond in the case of supported Pt_3Co and Pt_4 clusters and superoxo bond in the case of supported Pt_3Au cluster. Figures 5.8-5.9 show that the supported Pt_4 and Pt_3Au clusters easily accomplish the first half-reaction, via a series of metastable states (with no transition states), to the final product ($CO_2^{(g)} + O^*$) with the reaction energy -3.52 eV and -2.34 eV, respectively. Transforming one state to another, supported Pt_4 system involves a high barrier compared to the supported Pt_3Au system. The completely perturbed structure of the supported Pt_4 cluster was observed at the final step of the first half-reaction while the supported Pt_3Au cluster retains its pyramid structure at the final step (see Figure 5.9). On the other hand, the first transition state with an energy barrier of 0.76 eV and reaction energy of -2.01 eV (exothermic process) was detected for $Pt_3Co/Cu_2O(111)$ system during the first half L-H mechanism of CO oxidation with the slightly disturbed

structure of Pt_3Co cluster. The second half-reaction ($CO^* + O^* \rightarrow CO_2^{(g)}$) of the CO oxidation barrier is dependent on the breaking of the activated O bond to react with the next adsorbed CO to reach the final state ($CO_2^{(g)}$). We find that CO* and O* associate and form highly exothermic intermediate (with no transition state) i.e., the formation of CO_2^* with a 0.71 eV energy barrier in the second half-reaction on supported Pt_4 cluster. Subsequent CO_2 release, however, desires 0.53 eV for the supported Pt_4 cluster (see Figure 5.8). On the $Pt_3Au/Cu_2O(111)$ system, the second half-reaction to release the second CO_2 molecule proceeds through the TS with an energy barrier of 0.24 eV and reaction energy -0.88 eV (exothermic process). The co-adsorbed CO* and O* reacts to form a gas-phase CO_2 on the supported $Pt_3Co/Cu_2O(111)$ system and form an endothermic intermediate (0.58 eV) with a 0.83 eV activation barrier. Correspondingly release of CO_2 requires 1.10 eV for supported $Pt_3Co/Cu_2O(111)$. The strong co-adsorption of $CO^* + O^*$ on the supported Pt_4 and Pt_3Co cluster effectively leading to poisoning of the catalyst during the second half of the reaction. This is not detected for the supported Pt_3Au cluster, which exhibits the lowest energy barrier of 0.24 eV for the second half-reaction.

5.4 Conclusions

In summary, we have investigated the CO oxidation mechanisms on the $Cu_2O(111)$ supported Pt_4 and Pt_3X (X = Au and Co) clusters using first-principles based dispersion-corrected spin-polarized density functional theory calculations. It was observed that $Cu_2O(111)$ as support provides a good anchoring site for the clusters. Our calculations reveal that the support induces negative charge transfer to the clusters and that the effect is pronounced for the Pt_4 cluster and lessen for the Pt_3Co cluster. This trend is supported by the calculated binding energy of the cluster over $Cu_2O(111)$ support and plots of charge density distribution. A detailed analysis of the frontier orbitals has been summarized through the examination of the PDOS, which includes the contribution of s, p, and d orbitals components. As there is a one-to-one correspondence

of the *d-band* center and the CO adsorption strength, the *d-band* center and fractional filling of the *d-band* have been calculated for spin-up and spin-down states of the parent and doped metal atoms. The Au and Co sites were found more preferable for CO adsorption on $Pt_3Au/Cu_2O(111)$ and $Pt_3Co/Cu_2O(111)$ systems rather than Pt, expected to solve the critical problem of Pt poisoning. The trend of co-adsorption energy of CO + O_2 and CO + O on supported clusters is $Pt_3Co > Pt_4 > Pt_3Au$. The L-H reaction pathway obtained for the CO oxidation over considered systems indicates that supported Pt_4 and Pt_3Co clusters get easily poisoned by the strongly bound O atom and CO in the second half-reaction. However, the supported Pt_3Au cluster exhibits a smooth catalytic reaction profile for the first-half reaction and the lowest energy barrier of 0.24 eV in the second half-reaction of the CO oxidation. Hence, $Cu_2O(111)$ supported Pt_3Au cluster was spotted out as the most efficient cluster to eliminate the CO-poisoning. It is noted that the applicability of the considered *d-band* model is still debatable for Au-based systems and requires an accurate method to provide a reasonable explanation for the higher catalytic activity.

References

1. K. Liu, A. Wang, T. Zhang, *ACS Catal.* **2**, 1165-1178, (2012).
2. R. M. Heck, R. J. Farrauto, *Appl. Catal. A* **221**, 443-457, (2001).
3. H. J. Freund, G. Meijer, M. Scheffler, R. Schlogl, M. Wolf, *Angew. Chem. Int. Ed.* **50**, 10064-10094, (2011).
4. K. J. Hu, S. R. Plant, P. R. Ellis, C. M. Brown, P. T. Bishop, R. E. Palmer, *J. Am. Chem. Soc.* **137**, 15161-15168, (2015).
5. K. Yoon, Y. Yang, P. Lu, D. Wan, H. C. Peng, K. S. Masias, P. T. Fanson, C. T. Campbell, Y. A. Xia, *Angew. Chem. Int. Ed.* **51**, 9543-9546, (2012).
6. Z. Zhang, Y. Zhu, H. Asakura, B. Zhang, J. Zhang, M. Zhou, Y. Han, T. Tanaka, A. Wang, T. Zhang, et al., *Nat. Commun.* **8**, 16100-16110. (2017).
7. K. An, S. Alayoglu, N. Musselwhite, S. Plamthottam, G. Melaet, A. E. Lindeman, G. A. Somorjai, *J. Am. Chem. Soc.* **135**, 16689-16696, (2013).
8. L. Wang, J. Zhang, Y. Zhu, S. Xu, C. Wang, C. Bian, X. Meng, F. S. Xiao, *ACS Catal.* **7**, 7461-7465, (2017).
9. M. Haruta, T. Kobayashi, H. Sano, N. Yamada, *Chem. Lett.* **16**, 405-408, (1987).
10. R. Ahmad, A. K. Singh, *ACS Catal.* **5**, 1826-1832, (2015).
11. B. Yoon, H. Hakkinen, U. Landman, A. S. Worz, J. M. Antonietti, S. Abbet, K. Judai, U. Heiz, *Science* **307**, 403-407, (2005).
12. M. Valden, X. Lai, D. W. Goodman, *Science* **281**, 1647-1650, (1998).
13. I. X. Green, W. J. Tang, M. Neurock, J. T. Yates, *Science* **333**, 736-739, (2011).
14. H. Y. Kim, H. M. Lee, G. Henkelman, *J. Am. Chem. Soc.* **134**, 1560-1570, (2012).
15. M. F. Camellone, S. Fabris, *J. Am. Chem. Soc.* **131**, 10473-10483, (2009).
16. T. Yang, R. Fukuda, S. Hosokawa, T. Tanaka, S. Sakaki, M. Ehara, *ChemCatChem* **9**, 1222-1229, (2017).
17. R. Long, K. Mao, X. Ye, W. Yan, Y. Huang, J. Wang, Y. Fu, X. Wang, X. Wu, Y. Xie, et al., *J. Am. Chem. Soc.* **135**, 3200-3207, (2013).
18. J. D. Grunwaldt, C. Kiener, C. Wogerbauer, A. Baiker, *J. Catal.* **181**, 223-232, (1999).
19. M. Kuriyama, H. Tanaka, S. I. Ito, T. Kubota, T. Miyao, S. Naito, K. Tomishige, K. Kunimori, *J. Catal.* **252**, 39-48, (2007).
20. H. Q. Zhu, Z. F. Qin, W. J. Shan, W. J. Shen, J. G. Wang, *Catal. Today* **126**, 382-386, (2007).
21. H. Tanaka, M. Kuriyama, Y. Ishida, S. I. Ito, K. Tomishige, K. Kunimori, *Appl. Catal. A* **343**, 117-124, (2008).
22. Y. F. Han, M. J. Kahlich, M. Kinne, R. J. Behm, *Appl. Catal. B* **50**, 209-218, (2004).
23. B. Z. Sun, W. K. Chen, Y. J. Xu, *J. Chem. Phys.* **133**, 154502-154509, (2010).

24. D. F. Yancey, L. Zhang, R. M. Crooks, G. Henkelman, *Chem. Sci.* **3**, 1033-1040, (2012).
25. M. Ahmadi, F. Behafarid, C. Cui, P. Strasser, B. R. Cuenya, *ACS Nano* **7**, 9195-9204, (2013).
26. B. A. Baraiya, V. Mankad, P. K. Jha, *AIP, Conf. Proc.* **2115**, 030543-030547, (2019).
27. B. A. Baraiya, V. Mankad, P. K. Jha, *AIP, Conf. Proc.* **2265**, 030612-030616, (2020).
28. B. A. Baraiya, H. Tanna, V. Mankad, P. K. Jha, *J. Phys. Chem. A* **125**, 5256-5272, (2021).
29. J. R. Kitchin, J. K. Nørskov, M. A. Barteau, J. G. Chen, *Chem. Phys.* **120**, 10240-10246, (2004).
30. E. Christoffersen, P. Liu, A. Ruban, H. Skriver, J. K. Nørskov, *J. Catal.* **199**, 123-131, (2001).
31. B. Liu, Z. Zhao, G. Henkelman, W. Song, *J. Phys. Chem. C* **120**, 5557-5564, (2016).
32. X. L. Lei, M. S. Wu, G. Liu, B. Xu, C. Y. Ouyang, *J. Phys. Chem. A* **117**, 8293–8297, (2013).
33. M. Lykaki, E. Pachatouridou, S. A. C. Carabineiro, E. Iliopoulou, C. Andriopoulou, N. K. Kontos, S. Boghosian, M. Konsolakis, *Appl. Catal. B* **230**, 18-28, (2018).
34. Y. Yang, H. Dong, Y. Wang, C. He, Y. Wang, X. Zhang, *J. Solid State Chem.* **258**, 582-587, (2018).
35. Y. Yang, H. Dong, Y. Wang, Y. Wang, N. Liu, D. Wang, X. Zhang, *Inorg. Chem. Commun.* **86**, 74-77, (2017).
36. T. J. Huang, D. H. Tsai, *Catal. Lett.* **87**, 173-178, (2003).
37. B. Ma, C. Kong, J. Lv, X. Zhang, S. Yang, T. Yang, Z. Yang, *Adv. Mater. Interfaces* **7**, 1901643-1901651, (2020).
38. L. N. Wu, Z. Y. Tian, W. Qin, *Int. J. Chem. Kinet.* **50**, 507-514, (2018).
39. L. N. Wu, Z. Y. Tian, W. Qin, *J. Phys. Chem. C* **122**, 16733-16740, (2018).
40. P. Giannozzi, S. Baroni, N. Bonini, M. Calandra, R. Car, C. Cavazzoni, D. Ceresoli, G. L. Chiarotti, M. Cococcioni, I. Dabo, et al., *J. Phys. Condens. Matter* **21**, 395502-395521, (2009).
41. P. Giannozzi, O. Andreussi, T. Brumme, O. Bunau, M. B. Nardelli, M. Calandra, R. Car, C. Cavazzoni, D. Ceresoli, M. Cococcioni, et al., *J. Phys. Condens. Matter* **29**, 465901-465931, (2017).
42. S. Grimme, J. Antony, S. Ehrlich, H. A. Krieg, *J. Chem. Phys.* **132**, 154104-154122, (2010).
43. S. Grimme, S. Ehrlich, L. Goerigk, *J. Comput. Chem.* **32**, 1456-1465, (2011).
44. S. L. Dudarev, G. A. Botton, S. Y. Savrasov, C. J. Humphreys, A. P. Sutton, *Phys. Rev. B* **57,** 1505-1509, (1998).
45. L. I. Bendavid, E. A. Carter, *J. Phys. Chem. C* **117**, 26048-26059, (2013).

46. G. Kresse, D. Joubert, *Phys. Rev. B,* **59**, 1758-1775, (1999).
47. H. J. Monkhorst, J. D. Pack, *Phys. Rev.* **13**, 5188-5192, (1976).
48. N. Marzari, D. Vanderbilt, A. De. Vita, M. C. Payne, *Phys. Rev. Lett.* **82**, 3296–3299, (1999).
49. L. Li, R. Zhang, J. Vinson, E. L. Shirley, J. P. Greeley, J. R. Guest, M. K. Y. Chan, *Chem. Mater.* **30**, 1912-1923, (2018).
50. A. Werner, H. D. Hochheimer, *Phys. Rev. B* **25**, 5929-5934, (1982).
51. F. Chiter, D. Costa, V. Maurice, P. Marcus, *J. Phys. Chem. C* **124**, 17048-17057, (2020).
52. G. Henkelman, H. Jonsson, *J. Chem. Phys.* **113**, 9978-9985, (2000).
53. G, Henkelman, B. P. Uberuaga, H. A. Jonsson, *J. Chem. Phys.* **113**, 9901-9904, (2000).
54. N. Gupta, H. K. Machhi, B. A. Baraiya, S. S. Soni, A. V. Bedekar, P. K. Jha, H. P. Soni, (2021). DOI: 10.1021/acsanm.1c01169.
55. Y. Su, H. Li, H. Ma, J. Robertson, A. Nathan, *ACS Appl. Mater. Interfaces* **9**, 8100-8106, (2017).
56. B. Hammer, J. K. Nørskov, *Adv. Catal.* **45**, 71-129, (2000).
57. S. Bhattacharjee, U. V. Waghmare, S. C. Lee, *Sci. Rep.* **6**, 35916-35926, (2016).
58. M. Moseler, M. Walter, B. Yoon, U. Landman, V. Habibpour, C. Harding, S. Kunz, U. Heiz, *J. Am. Chem. Soc.* **134**, 7690-7699, (2012).
59. S. Kunz, F. F. Schweinberger, V. Habibpour, M. Rottgen, C. Harding, M. Arenz, U. Heiz, *J. Phys. Chem. C* **114**, 1651-1654, (2010).
60. L. Ma, M. Melander, T. Weckman, K. Laasonen, J. Akola, *J. Phys. Chem. C* **120**, 26747-26758, (2016).
61. L. Ma, K. Laasonen, J. Akola, *J. Phys. Chem. C* **121**, 10876-10886, (2017).